Simulation of emission spectra from nonuniform reactive laser-induced plasmas

Jörg Hermann*
LP3, CNRS - Aix-Marseille University, 13288 Marseille, France

Antonella Lorusso, Alessio Perrone, and Francesco Strafella
Università del Salento, Dipartimento di Matematica e Fisica and Istituto Nazionale di Fisica Nucleare, 73100 Lecce, Italy

Christophe Dutouquet
Institut National de l'Environnement Industriel et des Risques (INERIS/DRC/CARA/NOVA), 60550 Verneuil-En-Halatte, France

Béatrice Torralba
Centre Technique des Industries de la Fonderie (CTIF), 92318 Sèvres, France
(Received 17 July 2015; published 9 November 2015)

We demonstrate that chemical reactions leading to the formation of AlO radicals in plasmas produced by ablation of aluminum or Ti-sapphire with ultraviolet nanosecond laser pulses can be predicted by the model of local thermodynamic equilibrium. Therefore, emission spectra recorded with an echelle spectrometer and a gated detector were compared to the spectral radiance computed for uniform and nonuniform equilibrium plasmas. The calculations are based on analytical solutions of the radiation transfer equation. The simulations show that the plasmas produced in argon background gas are almost uniform, whereas temperature and density gradients are evidenced in air. Furthermore, chemical reactions exclusively occur in the cold plume periphery for ablation in air. The formation of AlO is negligible in argon as the plasma temperature is too large in the time interval of interest up to several microseconds. Finally, the validity of local thermodynamic equilibrium is shown to depend on time, space, and on the elemental composition. The presented conclusions are of interest for material analysis via laser-induced breakdown spectroscopy and for laser materials processing.

DOI: 10.1103/PhysRevE.92.053103 PACS number(s): 52.65.−y, 78.20.Bh, 82.60.Hc, 82.80.−d

I. INTRODUCTION

Plasmas produced by the interaction of intense laser pulses with matter have been investigated for more than five decades. During the early studies, ruby and CO_2 laser sources have been employed to explore the transformation of solids or gases in high-temperature plasmas [1]. The mechanisms of optical breakdown, in particular the contributions of avalanche ionization and multiphoton absorption, were ascertained [2]. At that time, the experimental techniques were limited to the collection of electrical charges, the characterization of shock waves via acoustical signals, and time-integrated recording of emission spectra [3,4]. Later, streak cameras were available to characterize the expansion dynamics of laser-produced plasmas [5]. With the diversification of the laser sources and the potential applications, the spreading of experimental conditions occurred. Given the great number of involved parameters, laser-matter interactions were investigated in a large variety of experimental conditions. In the 1980s, reliable laser Nd:YAG and excimer nanosecond laser systems were commercially available, leading to an increased development of applications, in particular in the field of materials science [6]. Laser processing, such as pulsed laser deposition of thin films [7], direct surface treatment [8], or cleaning [9], became popular. At the same time, the technological progress in the development of gated detectors gave access to time-resolved observations [10], and the increase of computational power pushed the development of numerical models describing laser-matter interactions [11–14]. In the past two decades, reliable mode-locked short pulse laser systems became commercially available, and new applications emerged [15]. In parallel, microscopic modeling techniques such as Monte Carlo simulation and molecular dynamics became accessible to describe the expansion dynamics of laser-produced plumes [16,17].

Basically, the existing theoretical approaches of laser ablation plumes can be classified into three categories according to the pressure of the surrounding background gas P_{gas} [18]. (i) At low pressure ($P_{gas} < 10^1$ Pa), the interaction of the ablated vapor with the surrounding gas occurs through diffusion and collective processes are negligible. Appropriate modeling is possible by dividing the process into two successive stages, the plume formation followed by the propagation through the background gas. (ii) At high pressure ($P_{gas} > 10^2$ Pa), collective processes dominate and lead to the formation of shock waves. The so-called *blast wave* or *point explosion* model proposed by Sedov [19] can be used to describe the expansion dynamics analytically. Here, heat and particle diffusion are neglected. (iii) In the intermediate pressure range, both collective and noncollective processes occur and the plume-gas mass and energy exchanges should be taken into account. The phenomenological description via the so-called *drag force* was proposed for that regime [20]. However, diffusive processes are not satisfactorily described by the continuous gas dynamics as the mixing of ablated species with the background gas is omitted. Alternatively, microscopic modeling accounts for diffusive processes. However, it requires large computational power, limiting thus the number of considered atoms or monomers. Hence hybrid models have

*hermann@lp3.univ-mrs.fr

been proposed to describe separately the early stage using a gas dynamical description, and the late stage by a microscopic model [18,21]. The above-mentioned classification according to the background pressure is a rough simplification, as the roles of collective and noncollective processes depend on the local number densities of ablated vapor and ambient gas species, and on the considered time scale. The characteristic time of interest is crucial for the relative importance of the processes. As a general rule, with increasing pressure, diffusion processes occur on a longer time scale. Thus, even at atmospheric background pressure, heat and particle diffusion become significant if the considered time scale is large enough.

The nature of ambient gas has a strong influence on the properties of laser-induced ablation plumes. For example, numerous studies of laser ablation under atmospheric pressure evidenced that, compared to ablation in ambient air, plasmas produced in rare gas atmospheres are brighter [22–24], characterized by larger values of temperature and electron density [25,26], and exhibit a longer lifetime [27]. In addition, the plasma generated in argon appears spatially more uniform, whereas temperature and density gradients have been evidenced for ablation in air, even at early times [28].

From the experimental point of view, space-resolved characterizations are difficult due to the small size of laser-produced plasmas and their fast expansion dynamics. The short lifetime restricts the observation to the most intense spectral lines that are often affected by self-absorption [29]. The optical thickness related to the large number densities of plasma species hinders the access to the inner plasma volume. In particular, the exploration of space-resolved measurements via Abel inversion implies an elaborated data treatment in which self-absorption is often ignored [30].

The gated charge-coupled device matrix detectors made spectral imaging techniques popular for the characterization of the expansion dynamics of laser-produced plasmas. We can distinguish two types of spectral imaging. (i) Imaging the laser plasma on the entrance of a monochromator so that the recorded data matrix has one spatial and one spectral axis [31,32]. (ii) Using narrow band filters, two-dimensional images of selected plasma species can be obtained [33,34]. The latter imaging technique gives more rapid access to the expansion behavior of a given plasma species. It is however difficult to evaluate the optical thickness of the observed spectral emission.

Information on the spatial distribution of plasma species during laser ablation at atmospheric pressure is of particular interest for elemental analysis via laser-induced breakdown spectroscopy (LIBS). Indeed, the so-called *calibration-free* LIBS measurements based on modeling of plasma emission have attracted a strongly growing interest in the past years [35–42]. These methods enable quantitative analysis without any requirement of preliminary calibration with matrix-matched standards. Different approaches have been proposed. The first and mostly applied calibration-free LIBS measurement procedure proposed by Ciucci *et al.* [43] is based on four hypotheses. (i) The ablation process is stoichiometric. (ii) The plasma is in local thermodynamic equilibrium. (iii) The plasma is spatially uniform and (iv) absorption of radiation by the plasma is negligible. The requirements of uniformity and negligible absorption being the most severe restrictions, several alternative approaches or improvements have been proposed [44–47].

In a recent paper, Shabanov and Gornushkin [48] applied a model based on the Navier-Stokes equations to describe the plume expansion into different inert background gases. The model predicts a maximum of mass density close to the vapor-gas contact front, and a strongly reduced mass density in the inner volume of the expanding vapor for times as large as a microsecond. These predictions seem to disagree with several experimental investigations that exhibit a maximum electron density in the center volume of the plasma [31,49]. Ma *et al.* [50] characterized the spatial distributions of spectral line emission from the ablated vapor and ambient gas atoms for laser ablation in argon. The authors observed efficient vapor-gas interdiffusion for ablation with infrared laser pulses. Contrarily, the absence of vapor-gas mixing was evidenced when using ultraviolet (UV) laser radiation.

The role of chemical reactions in atmospheric laser-produced plasmas was recently investigated by several groups [51–54]. A better knowledge of the chemical processes is motivated by the growth of functionalized nanoparticles [55], calibration-free LIBS measurements [56], and also by isotopic measurements [57,58].

In the present work, we investigate the role of chemical reactions during laser ablation in air and argon by comparing the measured emission spectrum to the spectral radiance of a plasma in local thermodynamic equilibrium. The calculation of the plasma composition includes the formation of diatomic species, and the spectral radiance of molecular emission bands is computed in addition to that of atomic lines. Aluminum oxidation was chosen as a model reaction, as precise spectroscopic data are available in literature for all involved plasma species.

II. MODELING

A. Calculation of the spectral radiance

Material ablation with pulsed lasers in a background gas at near atmospheric pressure leads to almost spherical expansion if the interaction of the laser beam with the gas is negligible, and the laser spot diameter is small compared to the plasma radius. In that case, the blast wave model may be applied to describe the plume expansion dynamics. The conditions are fulfilled for UV nanosecond laser pulses [59,60]. For infrared nanosecond pulses and irradiances typically applied in laser-induced breakdown experiments, the laser beam absorption by the background gas may lead to a preferential propagation of the plume along the laser beam axis, leading to an elongated plasma shape [59]. A simplified schematic view of a plasma produced by UV nanosecond pulses is displayed in Fig. 1(a). The plume is approximated by a hemispherical shape. To consider the spatial variations of temperature and densities, the plasma is divided into two zones: the plasma core and the peripheral zone. For laser ablation in ambient air, the peripheral zone is typically colder than the plasma core, due to the interaction with the background gas. Each plasma zone is approximated by its proper thermodynamic

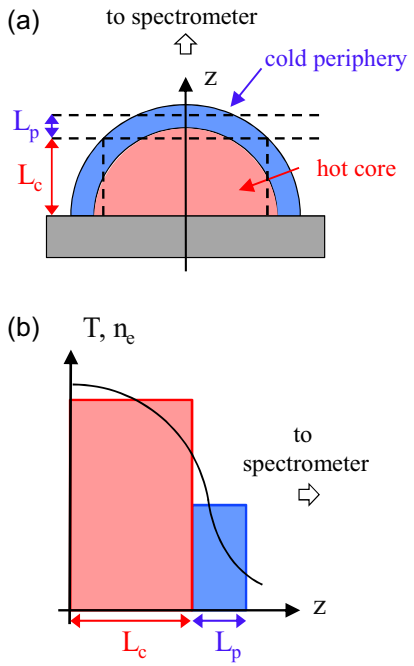

FIG. 1. (Color online) (a) Scheme of the hemispherical ablation plume composed of hot core and cold periphery. (b) Approximate description of spatial distributions of plasma properties by two zones of different thermodynamic state.

state as illustrated in Fig. 1(b). With respect to the uniform approximation, the additional zone may be considered as a first order correction that increases the accuracy of the calculation of the plasma emission spectrum. If the cold peripheral zone only weakly contributes to the plasma emission and mostly intervenes through absorption, we may further simplify the radiation model. By approximating the hemispherical figure by a rectangular shape as indicated on Fig. 1(a), the spectral radiance (radiation power per unit wavelength per unit solid angle per unit area) can be computed using an analytical solution of the radiation transfer equation. For observation in z direction (see Fig. 1) and assuming a plasma in local thermodynamic equilibrium, we have [61]

$$I_\lambda = U_p(1 - e^{-\tau_p}) + U_c(1 - e^{-\tau_c})e^{-\tau_p}, \tag{1}$$

where U is the blackbody spectral radiance and τ the optical thickness that characterizes the transmittance of the optical medium. The subscripts p and c stand for the core and peripheral plasma zones, respectively. The optical thickness is given by $\tau = \int \alpha(z)dz = \alpha L$, where L is the diameter of the plasma zone along the observation direction (see Fig. 1) and α the absorption coefficient given by [62]

$$\alpha(\lambda) = \pi r_0 \lambda^2 f_{lu} n_l P(\lambda)(1 - e^{-hc/\lambda kT}). \tag{2}$$

Here, r_0 is the classical electron radius, h is the Planck constant, c is the vacuum light velocity, and f_{lu} and n_l are the absorption oscillator strength and the lower level population number density of the transition, respectively. The normalized line profile $P(\lambda)$ is calculated considering Doppler and Stark broadening that are the dominant mechanisms of spectral line

TABLE I. Atomic mass m_A, ionization energies E_{ion} of neutral atoms and singly charged ions (superscript +), and atomic fractions of the constituents of the aluminum alloy C_{Al} and the Ti-sapphire crystal C_{Sa} (see Sec. III).

Elmnt.	m_A (amu)	E_{ion} (eV)	E^+_{ion} (eV)	C_{Al} (%)	C_{Sa} (%)
Al	26.98	5.98	18.83	92.7	40.0
O	16.00	13.62	35.12		60.0
Si	28.09	8.15	16.35	6.7	
Mg	24.30	7.65	15.04	0.5	
Fe	55.85	7.90	16.19	0.05	
Ti	47.90	6.83	13.58		
Sr	87.62	5.69	11.03	0.003	

broadening in strongly ionized laser-produced plasmas [49]. Depending on the relative values of Doppler and Stark width, the line shapes are described by Gaussian, Lorentzian, or Voigt profiles. The Doppler width is calculated according to plasma temperature and atomic mass (Table I) of the emitting species. The Stark width of each spectral line is obtained using the previously determined Stark broadening parameters w assuming a linear dependence of Stark width with the electron density [47,72]

$$\Delta\lambda_{\text{Stark}} = w\left(\frac{n_e}{n_e^{\text{ref}}}\right). \tag{3}$$

Here, n_e^{ref} is the reference electron density for which w is tabulated (see Table II). The Stark shift is obtained from Eq. (3) replacing w by the Stark shift parameter d.

For rotational lines of molecular spectra, Stark broadening was neglected as molecular emission bands are exclusively observed during the late stage of plume expansion, when the electron density is small. If the contribution of the cold peripheral zone to the plasma emission spectrum is negligible, Eq. (1) simplifies to the expression of the spectral radiance of a uniform plasma [73]

$$I_\lambda = U(1 - e^{-\tau}). \tag{4}$$

B. Molecular emission

Assuming local thermodynamic equilibrium, the population number density of a rotational level J in the vibrational level υ of the electronic state n is given by the Boltzmann law

$$n_{n,\upsilon,J} = n_{\text{mol}}\frac{g_{\text{tot}}}{Q_{\text{mol}}}e^{-[T_e+G_0(\upsilon)+F_\upsilon(J)]hc/kT}. \tag{5}$$

Here, n_{mol} and Q_{mol} are the number density and the partition function of the molecule, and T_e and $F_\upsilon(J)$ are the electronic and rotational terms, respectively. The vibrational term is referred to the lowest vibrational level $G_0(\upsilon) = G(\upsilon) - G(\upsilon = 0)$. The total statistical weight is given by $g_{\text{tot}} = g_e g_\upsilon g_J$, where g_e, g_υ, and g_J are statistical weights of the electronic, vibrational, and rotational levels, respectively. The statistical weight of the electronic state may be expressed as $g_e = (2S + 1)(2 - \delta_{0,\Lambda})$, where S is the quantum number of the electron spin and $\delta_{0,\Lambda}$ is the Dirac delta function that depends on the component of the electronic orbital momentum along the internuclear axis Λ. The $\delta_{0,\Lambda}$ function

TABLE II. Wavelength λ, transition probability A_{ul}, energy E, configuration, term and total angular momentum quantum number J of upper (index u) and lower (index l) excitation levels, Stark width w, and shift d for $n_e = 1 \times 10^{17}$ cm^{-3} of the selected transitions.

	λ	A_{ul}	E_l	E_u	Lower level			Upper level			w	d
Species	(nm)	(μs)	(eV)	(eV)	Config	Term	J_l	Config	Term	J_u	(pm)	(pm)
Al I	305.007	59.00[a]	3.60	7.67	$3s3p^2$	^{4}P	3/2	$3s3p(^3\text{P}^*)4s$	^{4}P*	5/2	29	16
Al I	305.468	78.00[a]	3.60	7.66	$3s3p^2$	^{4}P	1/2	$3s3p(^3\text{P}^*)4s$	^{4}P*	3/2	29	16
Al I	305.714	140.00[a]	3.61	7.67	$3s3p^2$	^{4}P	5/2	$3s3p(^3\text{P}^*)4s$	^{4}P*	5/2	29	16
Al I	305.903	28.00[a]	3.60	7.66	$3s3p^2$	^{4}P	3/2	$3s3p(^3\text{P}^*)4s$	^{4}P*	3/2	29	16
Al I	305.992	34.00[a]	3.60	7.65	$3s3p^2$	^{4}P	1/2	$3s3p(^3\text{P}^*)4s$	^{4}P*	1/2	29	16
Al I	306.429	160.00[a]	3.60	7.65	$3s3p^2$	^{4}P	3/2	$3s3p(^3\text{P}^*)4s$	^{4}P*	1/2	29	18
Al I	306.614	90.00[a]	3.61	7.66	$3s3p^2$	^{4}P	5/2	$3s3p(^3\text{P}^*)4s$	^{4}P*	3/2	29	18
Al I	308.215	58.70[b]	0.00	4.02	$3s^23p$	^{2}P*	1/2	$3s^23d$	^{2}D	3/2	75	21
Al I	309.271	72.90[c]	0.01	4.02	$3s^23p$	^{2}P*	3/2	$3s^23d$	^{2}D	5/2	75	21
Al I	309.284	11.60[d]	0.01	4.02	$3s^23p$	^{2}P*	3/2	$3s^23d$	^{2}D	3/2	75	21
Ti II	336.121	158.00[e]	0.03	3.72	$3d^2(^3\text{F})4s$	a^4F	7/2	$3d^2(^3\text{F})4p$	z ^{4}G*	9/2	12	
Fe I	358.119	102.00[f]	0.86	4.32	$3d^7(^4\text{F})4s$	a^5F	5	$3d^7(^4\text{F})4p$	z ^{5}G*	6	12	
Al II	358.656	235.00[g]	11.85	15.30	$3s3d$	^{3}D	3	$3s4f$	^{3}F*	4	110	1
Al II	358.707	209.00[g]	11.85	15.30	$3s3d$	^{3}D	2	$3s4f$	^{3}F*	3	110	1
Al II	358.745	197.00[g]	11.85	15.30	$3s3d$	^{3}D	1	$3s4f$	^{3}F*	2	110	1
Si I	390.552	13.30[h]	1.91	5.08	$3s^23p^2$	^{1}S	0	$3s^23p4s$	^{1}P*	1	47	24
Ca II	393.366	147.00[i]	0.00	3.15	$3p^64s$	^{2}S	1/2	$3p^64p$	^{2}P*	3/2	26	−6.3
Al I	394.401	49.90[d]	0.00	3.14	$3s^23p$	2P*	1/2	$3s^24s$	^{2}S	1/2	49	31
Al I	396.152	98.50[d]	0.01	3.14	$3s^23p$	^{2}P*	3/2	$3s^24s$	^{2}S	1/2	49	31
Sr II	407.771	141.00[j]	0.00	3.04	$4p^65s$	^{2}S	1/2	$4p^65p$	^{2}P*	3/2	36	−2.7
Al II	466.305	58.10[d]	10.60	13.26	$3p^2$	^{1}D	2	$3s4p$	^{1}P*	1	126	40
Mg I	518.360	56.10[d]	2.72	5.11	$3s3p$	^{3}P*	2	$3s4s$	^{3}S	1	90	45
Al II	623.175	84.00[g]	13.07	15.06	$3s4p$	^{3}P*	1	$3s4d$ Eq.	^{3}D	2	540	150
Al II	624.337	111.00[g]	13.08	15.06	$3s4p$	^{3}P*	2	$3s4d$	^{3}D	3	540	150
Al II	704.208	57.80[d]	11.32	13.08	$3s4s$	^{3}S	1	$3s4p$	^{3}P*	2	183	−25
Al II	705.671	57.40[d]	11.32	13.07	$3s4s$	^{3}S	1	$3s4p$	^{3}P*	1	183	−25

[a]Measured.
[b]Reference [63].
[c]Reference [64].
[d]Reference [65].
[e]Reference [66].
[f]Reference [67].
[g]Reference [68].
[h]Reference [69].
[i]Reference [70].
[j]Reference [71].

characterizes the so-called Λ-type doubling and we have $\delta_{0,\Lambda} = 1$ for $\Lambda = 0$ and $\delta_{0,\Lambda} = 0$ for $\Lambda > 0$. The statistical weights of vibrational and rotational levels are $g_\upsilon = 1$ and $g_J = g_N(2J+1)$, respectively. The nuclear statistical weight g_N accounts for the interaction with the nuclear spin. For heteronuclear molecules such as AlO, g_N is constant and can be ignored in the analysis of the molecular emission spectra. The vibrational and rotational terms $G_0(\upsilon)$ and $F_\upsilon(J)$ can be calculated using the term formula given by Herzberg [74] and the partition function is obtained by summing over all states

$$Q_{\text{mol}} = \sum_n g_e \sum_\upsilon \sum_J g_J e^{-[T_e + G_0(\upsilon) + F_\upsilon(J)]hc/kT}. \quad (6)$$

Assuming complete uncoupling of the rotational, vibrational, and electronic motions, the population number density of a rotational level is given by

$$n_{n,\upsilon,J} = n_{\text{mol}} \frac{g_{\text{tot}}}{Q_e(T_{el})Q_{\text{vib}}(T_{\text{vib}})Q_{\text{rot}}(T_{\text{rot}})} \times e^{-T_e hc/kT_{el}} e^{-G_0(\upsilon)hc/kT_{\text{vib}}} e^{-F_\upsilon(J)hc/kT_{\text{rot}}}. \quad (7)$$

Here, T_{el}, T_{vib}, and T_{rot} are the electronic, vibrational, and rotational excitation temperatures, and Q_e, Q_{vib}, and Q_{rot} are the electronic, vibrational, and rotational partition functions, respectively. The vibrational and rotational partition functions are computed for the most populated levels being the ground

state ($n = 1$) and the lowest vibrational level ($v = 0$). Due to the strong coupling of particles with similar mass, the electronic excitation temperature typically equals the temperature of free electrons in the plasma, whereas the vibrational and rotational temperatures equal the kinetic temperature of heavy particles T_h. Equation (7) enables calculations with fair accuracy if the population number densities of excited electronic states are small compared to the ground state population number density. Thus, for molecules having a large energy gap between the ground state and the first excited state, the partition function computed by the simplified expression can be used for moderate temperatures. In the case of AlO, the energy gap between the ground state and the first excited state is relatively small [75].

Using the superscripts $'$ and $''$ for the upper and lower electronic state, respectively, the absorption oscillator strength of a rotational line is given by

$$f_{J',J''} = f_{lu} q_{v',v''} \frac{H_{J',J''}}{2J''+1}. \quad (8)$$

Here, f_{lu} is the absorption oscillator strength of the electronic transition and $q_{v',v''}$ is the Franck-Condon factor for the transition from the vibrational level v' in the upper electronic state to the vibrational level v'' in the lower electronic state. The Hönl-London factor $H_{J',J''}$ can be calculated using the formula given by Kovács [76] for the corresponding type of transition. Inserting the absorption oscillator strength of the rotational line [Eq. (8)] and the corresponding lower level population density [Eq. (5) or Eq. (7)] in Eq. (2), we obtain the absorption coefficient of the rotational line. By summing over all rotational lines and using Eq. (1) or Eq. (4) we obtain the spectral radiance of molecular emission from a nonuniform or uniform plasma, respectively. Although these calculations are based on the assumption of local thermal equilibrium, they may be applied to plasmas with $T_h \neq T_{el}$ if the population number densities of electronic states follow the Boltzmann distribution and the influence of the heavy particle movement on the generated radiation power is small.

The AlO blue-green $B\,^2\Sigma^+ - X\,^2\Sigma^+$ system observed in the present study has a relative large transition probability [77]. It is easily observable and was extensively studied due to its importance in astrophysics [78–80]. According to the selection rules, the vibrational bands have two principal branches R and P corresponding to $\Delta J = J' - J'' = +1$ and $\Delta J = -1$, respectively (see Fig. 2). Moreover, two additional branches $^{R}Q_{21}$ and $^{P}Q_{12}$ of significantly lower emission intensity occur for $\Delta J = 0$. They correspond to $\Delta N = N' - N'' = +1$ and $\Delta N = -1$, respectively, where N is the quantum number of the total orbital angular momentum. The term splitting due to coupling of the electron spin with the nuclear rotational angular momentum (Λ-type doubling) was calculated using the splitting constants given by Saksena *et al.* [81]. We stress that, even if the Λ-type doubling is not resolved by the spectroscopic apparatus for small J values, the precise calculation of the rotational line positions is mandatory if absorption is significant. The upper and lower electronic levels being $^2\Sigma$ states, we used the term formula for doublets in Hund's case (b) to calculate the rotational terms [82]. The Franck-Condon factors used for the calculations were taken from Londhe *et al.* [83].

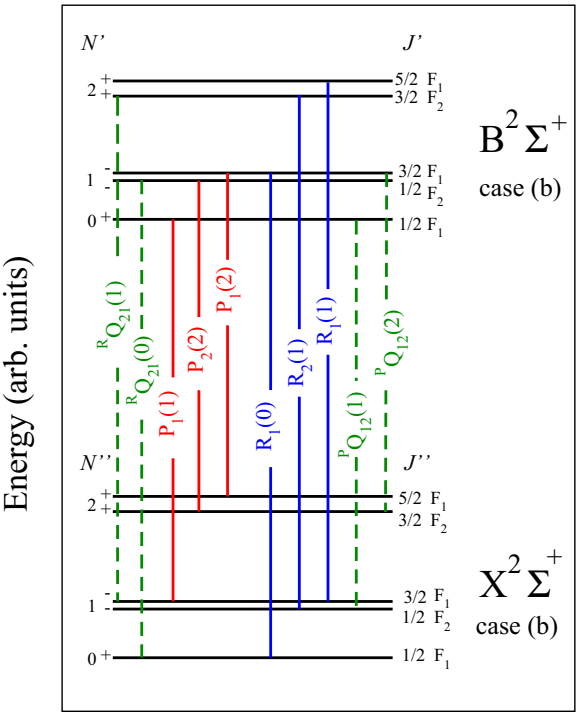

FIG. 2. (Color online) Energy level diagram of the AlO blue-green system. The contribution of the satellite branches $^{R}Q_{21}$ and $^{P}Q_{12}$ to the emission is weak and limited to the spectral range close to the band origin.

C. Chemical composition of the plasma

Plasmas produced by pulsed laser ablation at atmospheric pressure with irradiances much larger than the thresholds of material ablation and plasma ignition are strongly ionized. For experimental conditions applied in laser-induced breakdown spectroscopic experiments, electron densities of the order of 10^{18} and 10^{17} cm^{-3} are typically measured for delays of 100 ns and 1 μs after the laser pulse, respectively. In these conditions, collisional processes dominate and the population number densities of plasma species are expected to follow Boltzmann equilibrium distributions [84]. The plasma may be considered as quasistationary and characterized by the statistical laws of local thermodynamic equilibrium (LTE). Although the equilibrium state in LIBS plasmas is still a subject of controversy [85], the success of calibration-free measurements indicates that the assumption of LTE or partial LTE is valid in many cases. In particular, Boltzmann distributions of excited states are easily established in metal atoms as they possess many excited states, separated by relatively small energy gaps. Contrarily, atoms such as carbon, hydrogen, or oxygen have large energy gaps and impose larger electron densities to establish the Boltzmann equilibrium. The composition of a plasma in LTE composed of M elements depends on $M + 1$ parameters: the temperature and the atomic number densities of the M elements. In the temperature range of interest the formation of polyatomic molecules can be neglected and the atomic number density of an element A is given by

$$n_A = \sum_{z=0}^{z_{\max}} n_A^z + 2\sum_{z=0}^{1} n_{A_2}^z + \sum_{B\neq A}\sum_{z=0}^{1} n_{AB}^z. \quad (9)$$

Here, n_A^z and $n_{A_2}^z$ are the number densities of atomic and homonuclear diatomic species of charge z, respectively, and n_{AB}^z are the number densities of heteronuclear diatomic species of charge z formed by chemical reactions with the element B. The sum includes all species of significant abundance up to the maximum charge $z_{\max}$. The number densities of diatomic molecules formed by chemical reactions between the elements A and B were obtained from the Guldberg-Waage law of mass action for chemical equilibrium [86]

$$\frac{n_A^0 n_B^0}{n_{AB}^0} = \frac{(2\pi\mu kT)^{3/2}}{h^3}\frac{Q_A^0 Q_B^0}{Q_{AB}^0} e^{-D_0/kT}, \tag{10}$$

where n_A^0 and n_B^0 are the number densities of neutral atoms of elements A and B, respectively, and n_{AB}^0 is the density of diatomic molecules formed by chemical reactions between both elements. Q_A^0, Q_B^0, and Q_{AB}^0 are the corresponding partition functions. D_0 is the dissociation energy of the diatomic molecule AB in the ground state and $\mu = m_A m_B/(m_A + m_B)$ is the reduced mass. Thus, for given values of temperature and atomic number densities n_A of the M elements, the number densities of all plasma species can be calculated by numerically solving the equations that govern the LTE plasma [87]. Once the number densities of all species are calculated, the electron density is obtained from the equation of charge neutrality by summing the densities of all charged particles,

$$n_e = \sum_A \sum_{z=1}^{z_{\max}} z n_A^z. \tag{11}$$

For practical applications, the atomic number densities n_A [see Eq. (9)] of the M elements can be replaced by an equivalent set of input parameters: the electron density and the atomic or mass fractions of $M-1$ elements. The atomic fraction of each element C_A is obtained by dividing n_A by the sum over the atomic number densities of all elements $n_{\text{tot}} = \sum_A n_A$:

$$C_A = n_A/n_{\text{tot}}. \tag{12}$$

Substituting the number densities in Eq. (12) by the corresponding mass densities, we obtain the mass fractions of elements. The number densities of plasma species computed for local thermodynamic equilibrium are displayed in Fig. 3 for the elemental compositions of the here investigated aluminum alloy (a) and the Ti-sapphire sample (b). The calculations have been performed by setting the kinetic pressure of the plasma

$$P = \left[n_e + \sum_A \sum_{z=0}^{z_{\max}} \left(n_A^z + n_{A_2}^z + \sum_{B\neq A} n_{AB}^z \right) \right] kT - \Delta P \tag{13}$$

to atmospheric pressure. In Eq. (13), ΔP is the Debye pressure correction that accounts for the potential energy of charged species in the plasma. The pressure correction varies from about 0.1% to 40% of the kinetic pressure when the temperature rises from 4000 to 10 000 K. As the pressure is kept constant, the atomic number densities of elements and thus the total atomic number density of the plasma decrease with increasing temperature. For the aluminum alloy [Fig. 3(a)], only plasma species from the most abundant elements are displayed. According to the similar

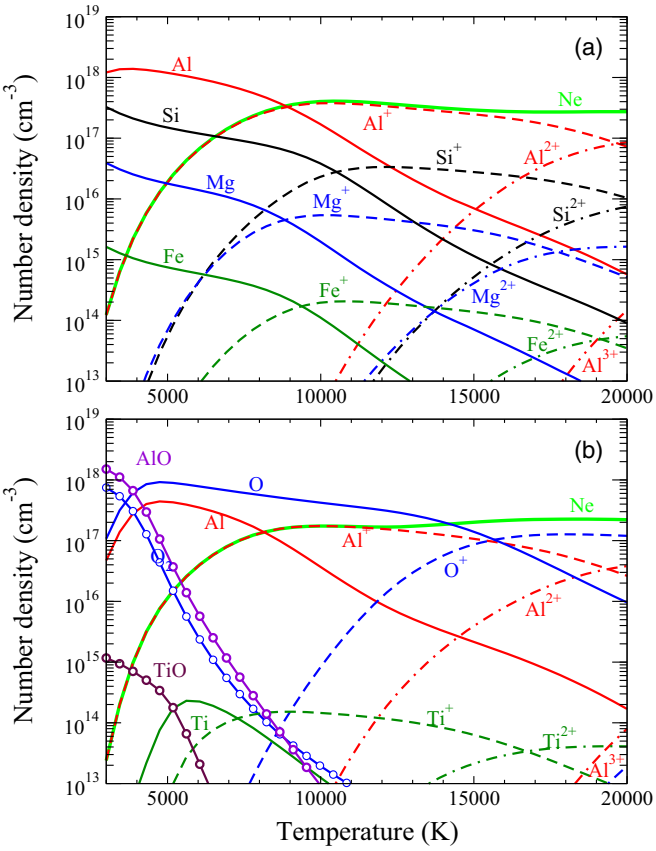

FIG. 3. (Color online) Number densities of species vs temperature computed for a plasma in local thermodynamic equilibrium at atmospheric pressure with the elemental composition of the aluminum alloy (a) and the Ti-sapphire crystal (b) (see Table I).

values of ionization energies of all elements (see Table I), the relative abundance of species with equal charge have analog temperature dependence: for $T \leqslant 8000$ K, neutral atoms are the most abundant plasma species, whereas singly charged ions dominate at larger temperature. For $T \leqslant 15\,000$ K, the electron density equals the number density of singly charged ions of the matrix element (Al). At larger temperature, doubly charged ions contribute to the plasma ionization as their relative abundances become significant. For Ti-sapphire (b), the temperature dependence of plasma species strongly differs from that of aluminum in the low-temperature range. The presence of oxygen leads to efficient oxidation and aluminum-oxide radicals dominate the plasma composition for $T \leqslant 4000$ K. However, the abundance of AlO rapidly decreases with temperature and can be neglected for $T > 7000$ K. Due to the large ionization energy of oxygen atoms, the contribution of oxygen to the plasma ionization is negligible for $T < 13\,000$ K.

The influence of temperature on the plasma emission spectrum is illustrated in Fig. 4 where the optical thickness (black line) and spectral radiance [red (gray) line] of a uniform plasma are displayed. The calculations were performed using Eqs. (2) and (4) for $L = 1$ mm and an elemental composition close to that presented in Fig. 3(b). The only difference relies in the absence of titanium that was omitted for simplification. The spectra (a), (b), (c), and (d) correspond to temperatures

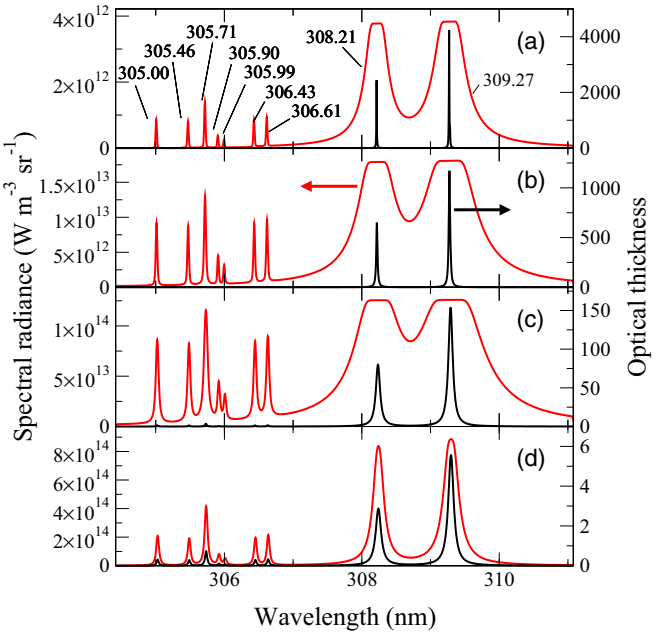

FIG. 4. (Color online) Spectral radiance [red (gray) curves] and optical thickness (black curves) computed for an Al_2O_3 plasma at atmospheric pressure assuming LTE. The calculation was made for temperatures of 4500 (a), 6000 (b), 8000 (c), and 12000 K (d) and a plasma diameter of 1.0 mm along the axis of observation (z axis in Fig. 1). The spectral range shows transitions of Al neutral atoms (see Table II).

of 4500, 6000, 8000, and 12 000 K, respectively. The corresponding values of number densities and partition functions of the most abundant plasma species are given in Tables III and IV, respectively. We observe multiplets of significantly different excitation energies in the presented spectral range. At low temperature (a) the optical thickness of the resonance lines Al I 308.21 and 309.27 nm is extremely large and the radiance of the higher excited transitions weak. With increasing temperature [(b)–(d)], the optical thickness of the resonance lines diminishes, and the spectral radiance of all transitions increases. Due to the electron density growth with T (see Table III), the Stark broadening of the lines increases. For the resonance lines, the broadening is strongly amplified by self-absorption leading to a maximum overlap of both transitions for $T = 8000$ K (c). At higher temperature (d), the width of the resonance lines diminishes dramatically although Stark broadening still increases. This is due to the lowering of optical thickness associated to the decrease of the number density of neutral atoms (see Table III). The saturation plateaus of the resonance lines observed for $T \leqslant 8000$ K (a)–(c) correspond to the blackbody spectral radiance [see Eq. (4)]. Even for $T = 12\,000$ K, when most of the aluminum atoms are ionized [see Fig. 3(b)] the optical thickness of the resonance lines is still significant. The temperature dependence of the line shapes illustrates the difficulties associated to the use of resonance lines for plasma diagnostics. These lines cannot be used for electron density measurements as Stark broadening is small compared to resonance broadening. The strong absorption makes also temperature measurements based on line-intensity ratios inefficient.

TABLE III. Number densities n of most abundant species, total number density of atoms $n_{\rm tot}$ [see Eq. (12)], and electron density n_e computed for an Al_2O_3 plasma at atmospheric pressure for various temperatures T. The number densities are given in 10^{16} cm^{-3}.

T (K)	n_{Al}	n_{Al^+}	$n_{Al^{2+}}$	n_O	n_{O_2}	n_{AlO}	$n_{\rm tot}$	n_e
4500	53.4	1.27		81.5		6.12	140	1.27
6000	42.9	4.22		70.7		0.67	118	4.23
8000	19.1	14.8		50.8		0.02	84.8	14.9
12000	1.17	18.2	0.02	28.2	0.93		48.6	19.0
15000	0.26	12.7	0.45	12.6	7.49		33.5	21.0

The spectral radiance [red (gray) line] and the optical thickness (black line) displayed in Fig. 5 for the spectral range from 443 to 560 nm were calculated for plasma conditions equal to those of Fig. 4. We observe the emission bands of the most intense vibrational sequences of the AlO blue-green system. It is shown that the optical thickness of the molecular bands is large at low temperature, with a maximum value $\cong$20 of the most intense band heads for $T = 4500$ K (a). Consequently, the shape of the observed rovibrational intensity distribution is altered compared to the optically thin case. When increasing the temperature from 4500 (a) to 6000 K (b), the number density of AlO molecules diminishes by almost one order of magnitude [see Fig. 3(b)]. Consequently, the optical thickness decreases by a factor of 10, and the spectral shape changes towards the optically thin shape. It is noted that the temperature variation from 4500 to 6000 K leads to a change of the (0,0) band head intensity by a factor of 1.3 only. This illustrates that the decrease of the AlO number density with T is partially compensated by the increase of excitation rate and the lowering of self-absorption. For $T = 8000$ K (c), the molecular emission bands are optically thin and their spectral radiance is small ($\leqslant$1%) compared to that of intense atomic lines [Fig. 4(c)]. For $T = 12\,000$ K [Fig. 5(d)], molecular emission is not detectable and ionic lines appear.

To illustrate the influence of self-absorption on the spectral shape of the molecular emission bands, we present in Fig. 6 the (1,0) and (2,1) bands in a narrow spectral window. With the exception of the wavelength range, the spectra are identical to those presented in Fig. 5. It is shown that the strong self-absorption for $T = 4500$ K [Fig. 6(a)] tends to reduce the band head intensity with respect to that of the band tail. As the tail is composed by rotational levels of large J values and thus large rotational energy, the rotational temperature (deduced from the intensity distribution of the rotational lines) may be overestimated if self-absorption is ignored.

III. EXPERIMENT

The experiments were carried out with a frequency-quadrupled Nd:YAG laser (Quantel, model Brilliant) delivering pulses of 4 ns duration and 40 mJ energy at the wavelength of 266 nm. The laser pulse energy was attenuated to 6 mJ by turning the beam polarization with the aid of a half-wave plate and crossing through a polarization analyzer. The laser beam was focused onto the sample surface using a plano-convex lens of 150 mm focal length. According to a spot diameter of 100 μm of the Gaussian beam, a laser fluence of about

TABLE IV. Ionization energy reduction according to Griem ΔE_{ion} [88], and partition functions Q of most abundant plasma species used for the calculations of the composition of an Al_2O_3 plasma at atmospheric pressure for different temperatures T (see Table III). The values of molecular partition functions in parentheses were obtained using the simplified expression based on the assumption of complete decoupling between rotational, vibrational, and electronic motions [see Eq. (7)].

T (K)	ΔE_{ion} (eV)	Q_{Al}	Q_{Al^+}	$Q_{Al^{2+}}$	Q_O	Q_{O^+}	Q_{O_2}		Q_{AlO}	
4500	−0.05	5.88	1.00	2.00	8.86	4.00	2.28	(2.22)	7.93	(6.62)
6000	−0.08	5.92	1.00	2.00	8.95	4.02	3.34	(3.21)	12.7	(10.3)
8000	−0.13	6.15	1.01	2.00	9.17	4.08	6.35	(5.97)	26.9	(20.7)
12000	−0.12	8.15	1.10	2.01	9.69	4.45	17.1	(15.0)	75.5	(57.4)
15000	−0.11	11.8	1.26	2.03	10.1	4.89	30.4	(25.4)	130	(102)

80 J cm^{-2} was obtained on the sample surface. Two samples were irradiated: (i) an aluminum alloy of 4 mm thickness and 25 × 25 mm^2 area manufactured by the technical center of French foundries (CTIF). The elemental composition of the alloy was measured using a wavelength-dispersive x-ray fluorescence spectrometer (Thermo electron, model 9400 XP). (ii) A Ti-sapphire disk of 2 mm thickness and 25 mm diameter. The samples were placed on a motorized sample holder in a vacuum chamber of 10^{-4} Pa residual pressure. During the experiments, the chamber was filled with either argon at 5×10^4 Pa pressure or air at atmospheric pressure.

The plasma emission was captured by imaging the plume with two lenses of 150 and 35 mm focal lengths onto the entrance of an optical fiber of 600 μm diameter. The optical axis of the lenses was tilted by 15° with respect to the surface normal. According to the image magnification of about 1:5, a cylindrical volume of about 3 mm diameter was observed. The fiber was coupled to the entrance of an echelle spectrometer (LTB, model Aryelle Butterfly) of 0.4 m focal length and a resolving power of 8.9×10^3. Photon detection was ensured using an intensified charge-coupled device matrix detector (Andor, model IStar). The spectral resolution of the apparatus was measured as a function of wavelength using a low-pressure argon-mercury lamp. An intensity calibration of the spectroscopic apparatus has been performed in the visible and UV spectral ranges using a calibrated tungsten lamp (Oriel, model 63358) and a deuterium lamp (Heraeus, model DO544J), respectively.

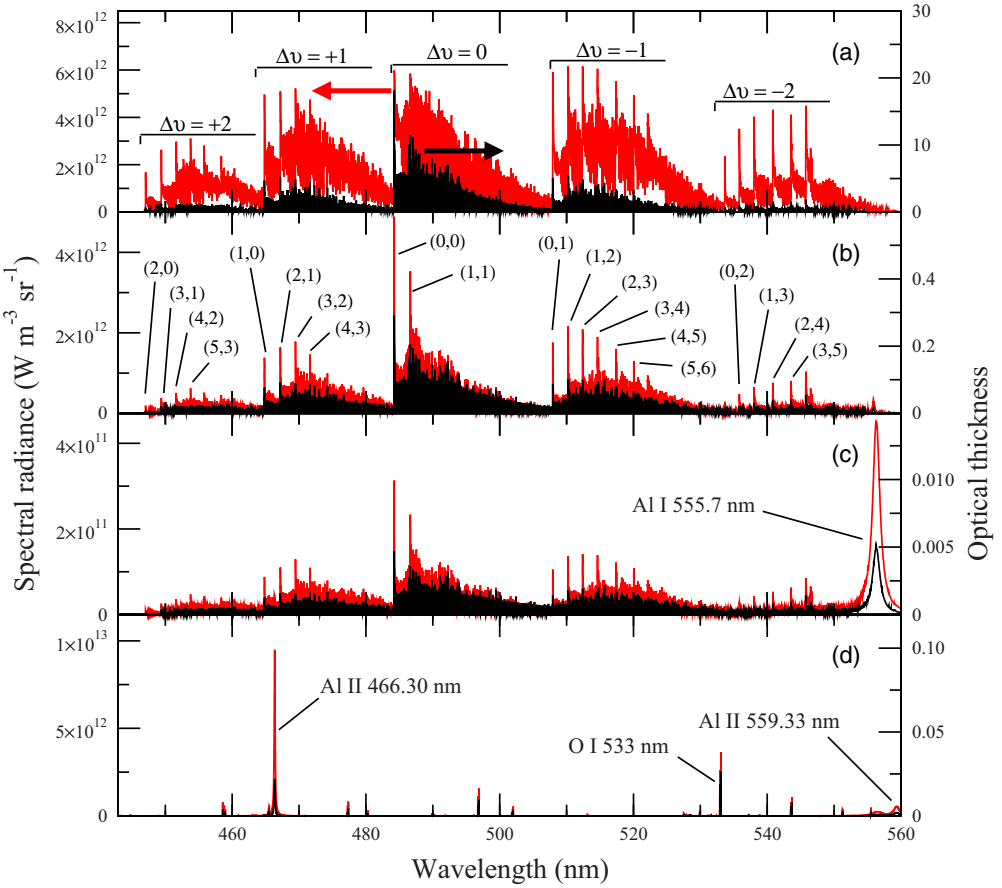

FIG. 5. (Color online) Spectral radiance [red (gray) curves] and optical thickness (black curves) computed for the range from 443 to 560 nm. Despite the range, the calculation parameters of (a)–(d) equal those of Figs. 4(a)–4(d).

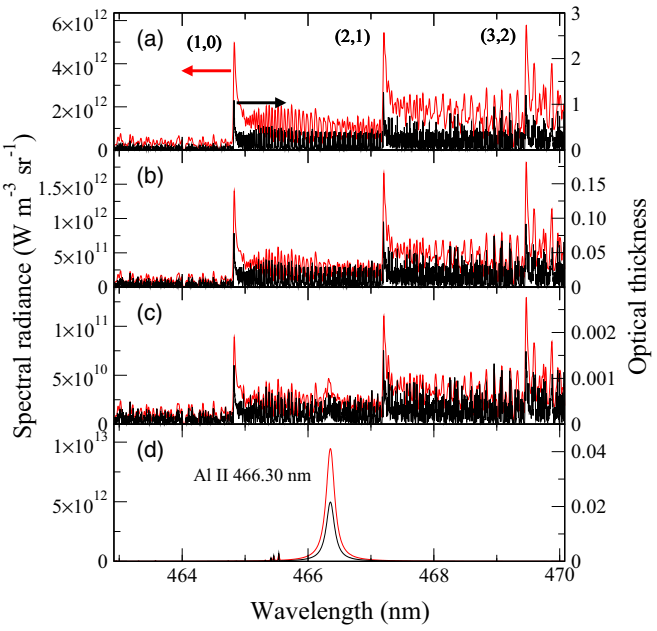

FIG. 6. (Color online) Spectral radiance [red (gray) curves] and optical thickness (black curves) computed for the range from 463 to 470 nm. Despite the range, the calculation parameters of (a)–(d) equal those of Figs. 4(a)–4(d) and 5(a)–5(d).

The spectra were recorded for different delays of the detector gate t_g with respect to the laser pulse. The gate width Δt_g was adjusted for each delay so that $\Delta t_g < t_g$. To enhance the signal-to-noise ratio, data acquisition was performed by averaging over 200 ablation events, applying 10 pulses on 20 different irradiation sites. The sites were separated by a distance of 150 μm. For measurements recorded with large delays, when the plasma brightness is low, the spectra recording was repeated 10 times to compensate for the lower signal-to-noise ratio. The experimental procedure was automated with the aid of a controller unit and appropriate software.

IV. RESULTS AND DISCUSSION

A. Diagnostics in argon: Database completion

Plasma diagnostics require accurate spectroscopic data that are unavailable or only partially available for atomic and ionic lines of many elements. Although aluminum transitions have been extensively studied, the transition probabilities A_{ul} reported in literature for several prominent lines suffer large uncertainties. For example, no A_{ul} values are given in the NIST database [65] for the lines situated between 305 and 307 nm. These transitions are of great interest, as their excitation energies are large compared to other observable lines of neutral aluminum (see Table II).

To overcome the problem related to missing or uncertain spectroscopic data, we performed spectroscopic recordings during laser ablation in argon for various delays between the laser pulse and the detector gate. These measurements take advantage of the spatially uniform character of the plasma produced by UV laser ablation in argon [89]. In that condition, the emission spectrum of the ablation plume is well described by Eq. (4) [28,90]. In Fig. 7, the measured and computed

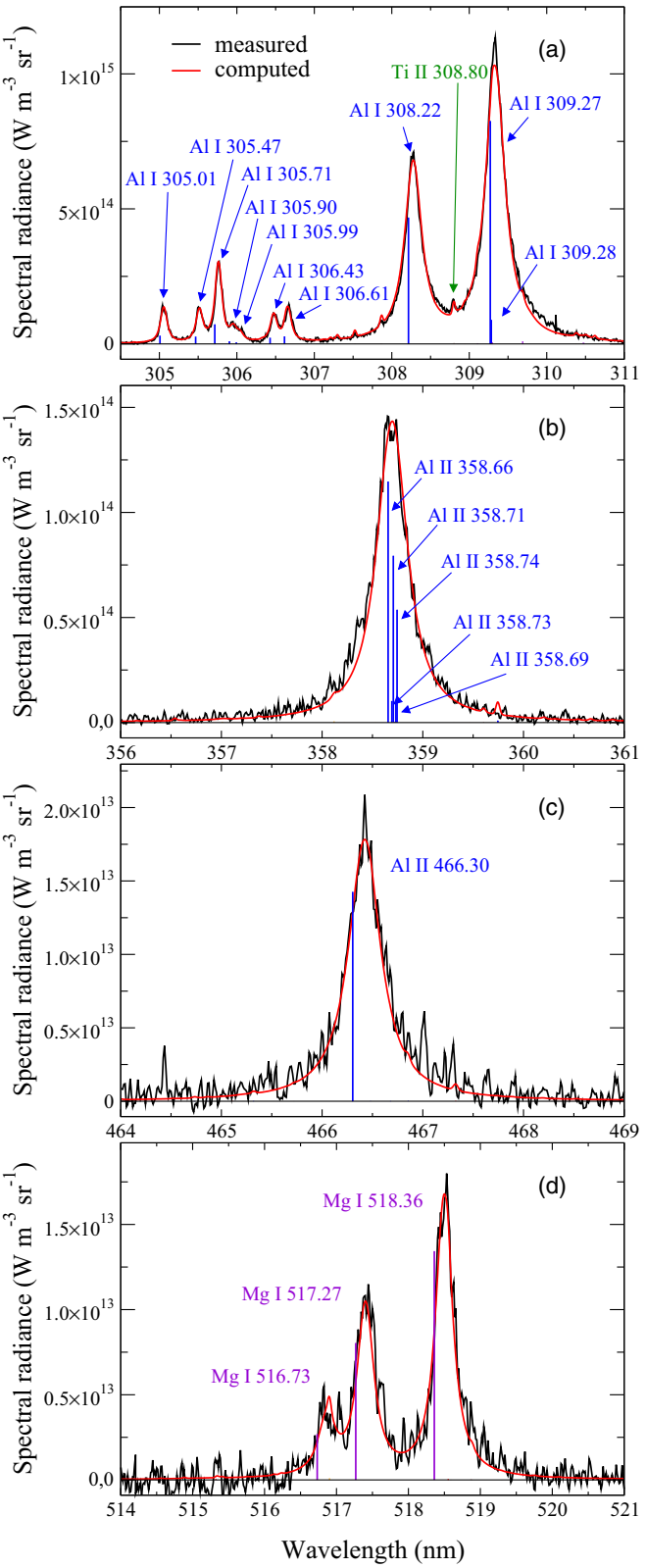

FIG. 7. (Color online) Measured (black lines) and computed [red (gray) lines] spectral radiance of transitions of Al (a), Al^+ (b), (c), and Mg (d). The recording was performed during ablation of the aluminum alloy in argon at 5×10^4 Pa pressure for $t = (500 \pm 100)$ ns.

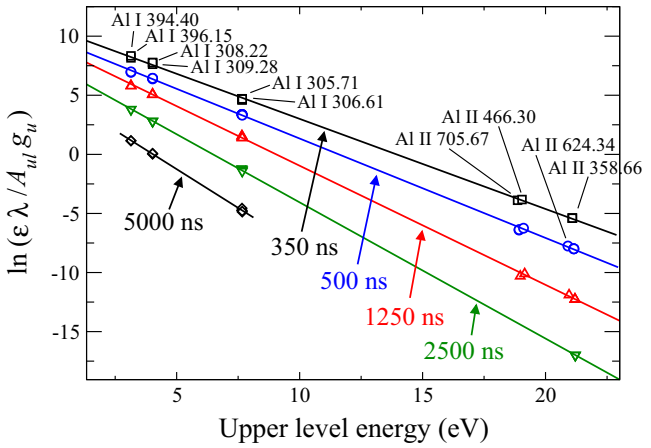

FIG. 8. (Color online) Saha-Boltzmann plot for ablation of aluminum in argon at 5×10^4 Pa pressure.

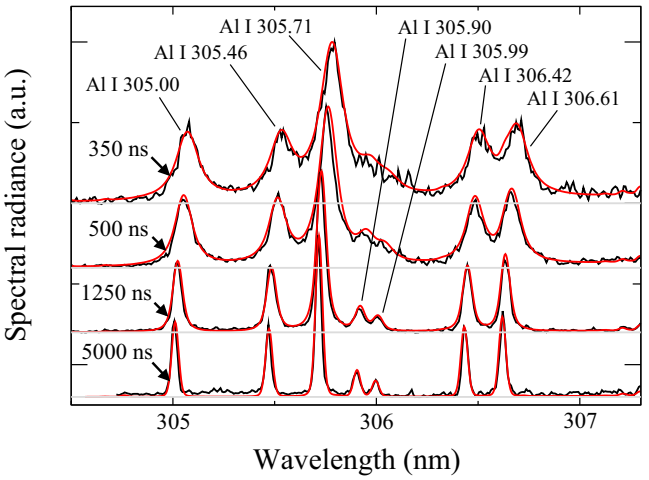

FIG. 9. (Color online) Measured (black lines) and computed [red (gray) lines] spectral radiance of Al transitions for ablation of aluminum in argon at 5×10^4 Pa pressure at different observation times.

spectra are displayed for several spectral ranges. The recording was performed with a gate delay $t_g = 400$ ns and a gate with $\Delta t_g = 200$ ns, corresponding to an observation time $t = (500 \pm 100)$ ns. An iterative calculation procedure is applied to deduce the plasma properties from the best agreement between measured and computed spectra [90]. The simulations were performed for various observation times to obtain a consistent set of data for the evaluation of Stark broadening parameters and transition probabilities. We assumed a linear dependence of the Stark widths on the electron density and neglected the temperature dependence of the broadening parameters.

The quality of the plasma diagnostics performed in argon is illustrated by the Saha-Boltzmann plot displayed in Fig. 8 for different measurement times. Here, $\epsilon_{ul}^{\text{meas}}$ is the emission coefficient deduced from the measurements using $\epsilon_{ul}^{\text{meas}} = \epsilon_{ul}^{\text{comp}} I_{\text{meas}}/I_{\text{comp}}$, where I_{meas} and I_{comp} are the measured and computed line-integrated spectral radiances, respectively. As the computed spectral radiance intrinsically accounts for self-absorption, the Saha-Boltzmann plot displayed in Fig. 8 is equivalent to the Boltzmann plot corrected for self-absorption presented by Bulajic *et al.* [44]. It is shown that the population number densities of atomic and ionic excited species are well described by the equilibrium distribution for all measurement delays. To obtain the good agreement for all presented spectral lines, the transition probabilities of the spectral lines presented in Fig. 9 were adjusted so that the deviations from the slopes in Fig. 8 were minimized for all delays. We stress that the deduced A_{ul} values (see Table II) differ by a factor of two from those reported by Kurucz and Peytremann [91] tabulated in the Kurucz database [92].

B. Time evolution in argon and air

The time evolutions of electron density and plasma temperature in argon at 5×10^4 Pa pressure and air at ambient pressure are presented in Fig. 10 for ablation of aluminum (a) and Ti-sapphire (b). The error of 20% of the n_e values is mainly due to the low accuracy of the Stark broadening parameters. To characterize the decrease of T and n_e, we approximated the measured data by functions $n_e, T = At^B$ (continuous lines) with the parameters A and B obtained from the best fit. It is shown that the n_e and T values measured in argon (empty symbols) are systematically larger than those measured in air (filled symbols). In addition, the decrease is faster in air. Comparing the observations for ablation of aluminum (a) and Ti-sapphire (b), it is observed that the difference between the decay rates observed in argon and air are stronger for Ti-sapphire. The behavior can be explained qualitatively by the expected principal loss rates of plume energy: after the initial quasiadiabatic expansion during the first 100 ns, the

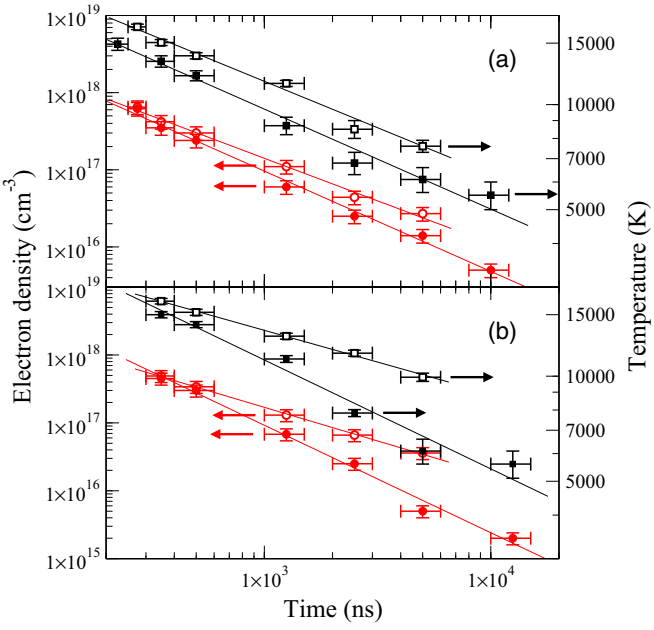

FIG. 10. (Color online) Electron density [red (gray) circles] and temperature (black squares) vs time measured for ablation of aluminum (a) and Ti:sapphire (b) in 5×10^4 Pa argon (empty symbols) and in ambient air (filled symbols). The vertical error bars represent the measurement uncertainties, whereas the horizontal error bars indicate the time of observation (gate width).

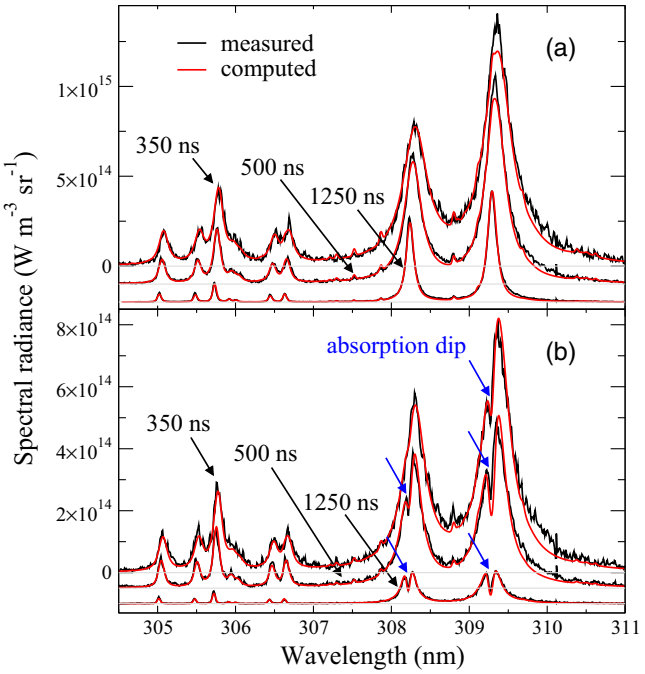

FIG. 11. (Color online) Measured (black lines) and computed [red (gray) lines] spectral radiance of Al transitions for ablation of aluminum in argon at 5×10^4 Pa pressure (a) and in air at ambient pressure (b) and different observation delays.

main losses of energy occur through radiation and energy exchange with the surrounding background gas [18,93]. The energy exchange with air molecules being more efficient than the exchange with atomic argon, the energy loss rate and thus the observed decays of T and n_e are smaller for the inert gas. Compared to oxygen atoms and ions, the metal plasma species have significantly richer emission spectra. Thus radiation losses are expected to be smaller for Ti-sapphire composed by 60% of oxygen atoms. For ablation of Ti-sapphire in argon, both loss terms are minimized, and the largest temperature values are observed at late times.

Spectra measured at different delays are presented in Fig. 11 for laser ablation in argon (a) and in air (b). They were compared to the spectral radiance computed for a plasma in local thermodynamic equilibrium. For ablation in argon (a), the measured spectrum was found to be well described by the spectral radiance of a uniform plasma [Eq. (4)], whereas the nonuniform description [Eq. (1)] was required for plasma emission produced in air (b). Neglecting segregation within the ablated vapor (equal elemental composition in both zones), the variable parameters are L, T, and n_e. In addition, the mixing of the ablated vapor with the air is introduced by adding large fractions of oxygen and nitrogen to the elemental composition of the peripheral layer (see Table V). It is shown that the aluminum resonance lines observed in air exhibit absorption dips at the resonance wavelength for all measurement delays. This feature is due to absorption of radiation from the hot plasma core by the colder peripheral zone. As the electron density in the peripheral zone is small, absorption occurs in a narrow range close to the resonance wavelength only. Due to the Stark redshift of spectral line emission from the plasma core (see Table II), the absorption dips occur on the blue side of the shifted line center. With increasing time, the electron density and thus the Stark shift decreases and the absorption dips appear closer to the line center. Comparing the spectral shapes of the resonance lines in argon (a) and air (b) we observe that the linewidths in air are larger, although the electron density is smaller [see Fig. 10(a)]. This is attributed to the lower plasma temperature and the subsequent stronger resonance broadening for ablation in air (see T dependence of optical thickness in Fig. 4).

TABLE V. Parameters of the two plasma zones used for the calculation of the spectrum displayed in Fig. 12: plasma diameter L, electron temperature T_{el}, heavy particle temperature T_h, electron density n_e, and fraction of atoms originating from the ambient air $n_{\text{air}}/(n_{\text{vap}} + n_{\text{air}})$. The total number density of atoms n_{tot} and the pressure P computed using Eq. (13) are given in the last rows.

	Plasma core	Peripheral zone
L (mm)	0.7	0.1
T_{el} (K)	6100	4500
T_h (K)	6100	4000
n_e (cm^{-3})	1.6×10^{16}	2.0×10^{15}
$n_{\text{air}}/(n_{\text{vap}} + n_{\text{air}})$		0.99
n_{tot} (cm^{-3})	7.3×10^{16}	1.4×10^{19}
P (Pa)	7.0×10^3	4.8×10^5

C. Role of chemical reactions

Molecular species are formed in strongly ionized plasmas with significant number densities if their dissociation energies are almost as large as the ionization energies of atoms. This is the case for AlO radicals ($D_0 = 5.25$ eV [75]) and the strong AlO blue-green system was currently observed in laser-produced plasmas [55,56,94]. According to the computed spectra shown in Figs. 5 and 6, the AlO emission bands are expected to be observable in atmospheric LTE plasmas composed of aluminum and oxygen for $T \leqslant 8000$ K. For temperatures below 6000 K, the AlO bands dominate the plasma emission spectrum and their absorption becomes significant. The self-absorption of the vibrational bands of the AlO blue-green system was reported by Lam *et al.* [95]. The authors ignored the band heads of large optical thickness and deduced the rotational temperature T_{rot} from the intensity distribution of the band tail only. The T_{rot} value was found to be smaller than the electronic excitation temperature of atoms and ions, and the gap between both temperatures persisted until times of several tens of microseconds. Ignoring possible spatial variations of temperature, the authors concluded that the plasma was out of equilibrium.

In the present work, the temperature gradients evidenced by the spectra recorded for $t \leqslant 1250$ ns [Fig. 11(b)] during laser ablation in ambient air were found to subsist for longer times. A spectrum recorded at $t = (5 \pm 1)$ μs is displayed in Fig. 12. The three spectral ranges show the aluminum resonance lines (a), and the $\Delta\upsilon = 0$ (b) and $\Delta\upsilon = -1$ (c) sequences of the AlO blue-green system. Similar to the observations at earlier time [Fig. 11(b)], the resonance lines exhibit absorption dips (a), proving the existence of a cold peripheral zone at the plume border. The spectral radiance computed for a nonuniform

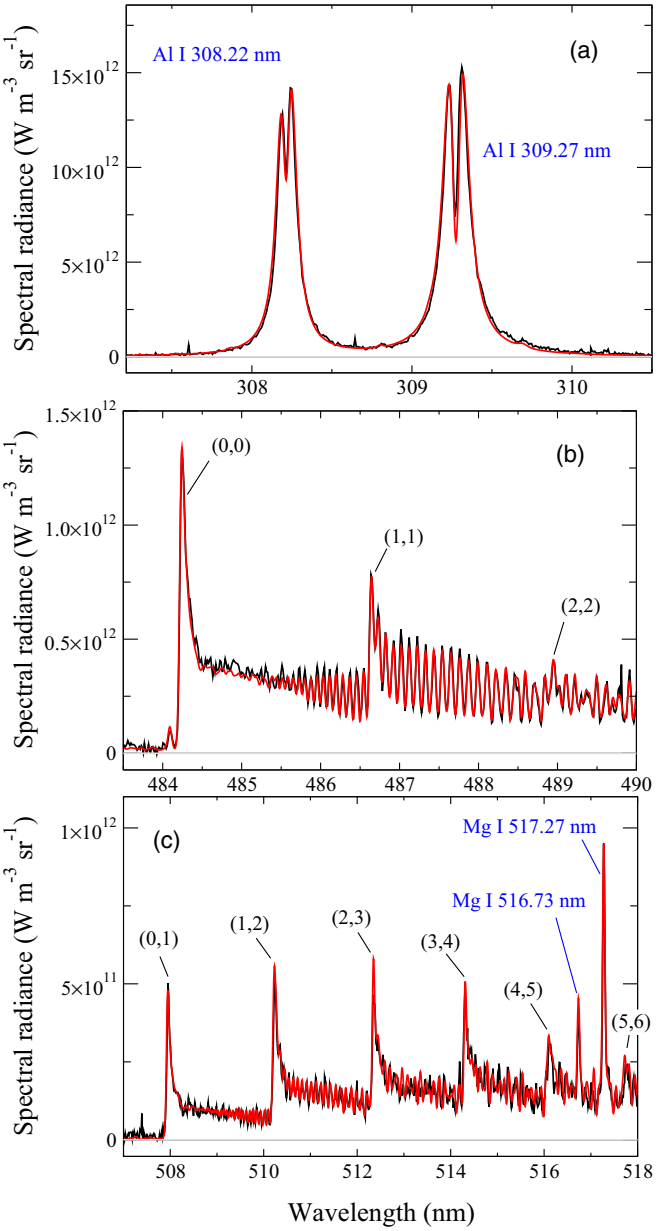

FIG. 12. (Color online) Measured (black lines) and computed [red (gray) lines] spectral radiance of aluminum resonance lines (a) and emission bands of the AlO blue-green system belonging to the $\Delta v = 0$ (b) and the $\Delta v = -1$ (c) vibrational sequences. The recording was performed during ablation of aluminum in ambient air for $t = (5 \pm 1)$ μs. The calculation was performed assuming a nonuniform plasma using the parameters listed in Table V.

plasma using Eq. (1) with the parameters given for both zones in Table V retraces closely the measured spectrum in all spectral ranges. The good agreement between measured and computed spectra supports the formation of strong gradients during ablation in air that persist over the entire lifetime of the plasma. Thus atomic and molecular emission originate from zones of different temperature, and the disparity between rotational temperature of molecules and electronic temperature of atoms does not prove the absence of local thermodynamic equilibrium. However, the simulation reveals that the rotational and electronic excitation temperatures slightly differ in the peripheral zone (see Table V). This mismatch may be attributed to the temperature difference between the hot plasma core and the cool surrounding background gas. Located between the hot core and the cold gas, the plume periphery exchanges energy with both zones. Due to the large electron density in the plasma core, electron heat transport from the core towards the periphery is expected. At the same time, large collision rates of heavy particles preferentially occur at the outer border of the peripheral zone, where the density of the compressed background gas is maximum [48]. These collisions tend to thermalize the heavy particles of the plume periphery with those of the cool surrounding gas. As a result, the plume periphery is characterized by heavy particle temperature inferior to the electron temperature. According to the McWhirter criterion [96], the failure of equilibrium in the plume periphery is also expected from the low electron density. The electron density being much larger in the plasma core, the loss of equilibrium in the colder plume periphery is not necessarily associated to a complete loss of equilibrium in the entire plume.

D. Determination of the elemental composition

To verify the validity of the model used for the simulation of the plasma emission spectra, we compared the elemental compositions deduced for both samples in argon and air to their reference values. The mass fractions of the most abundant elements of the aluminum alloy are presented in Fig. 13 for measurements in argon (a) and air (b). For each element, several values deduced from the LIBS analysis [colored (gray) columns] are compared to the reference data (black column). They have been obtained from the analysis of spectra recorded at different delays. The reference values were measured by wavelength-dispersive x-ray fluorescence spectroscopy (XRF). For titanium, the reference value is not given because its abundance was below the detection limit of the XRF measurements. We observe a fair agreement between the compositions measured by XRF and LIBS. The largest relative error of about 30% is observed for magnesium. The fluctuations between the elemental fractions measured by LIBS for different conditions are much smaller, although large variations of the plasma properties were observed during the time evolution from 350 ns to 5 μs. This supports the validity of the applied plasma model. In particular, it illustrates that the nonuniform character of the plasma formed in air can be ignored as long as lines of weak or moderate optical thickness are used for the analysis. Furthermore, the LIBS analysis of spectra recorded with large delays show that chemical reactions do not affect the plasma core, as the temperature is too high for their formation in the central volume of the plume. Thus molecular transitions may be ignored in LIBS measurements if they do not interfere with the atomic lines used for the analysis.

The elemental composition deduced from the LIBS analysis of the Ti-sapphire sample is presented in Fig. 14. To enable the measurement of the oxygen fraction, the analyses were performed in argon. The reference fractions of aluminum and oxygen correspond to stoichiometric sapphire (Al_2O_3). The fraction of titanium was unknown. It is shown that for spectra recording delays $\leqslant 1$ μs, the measured atomic fractions are

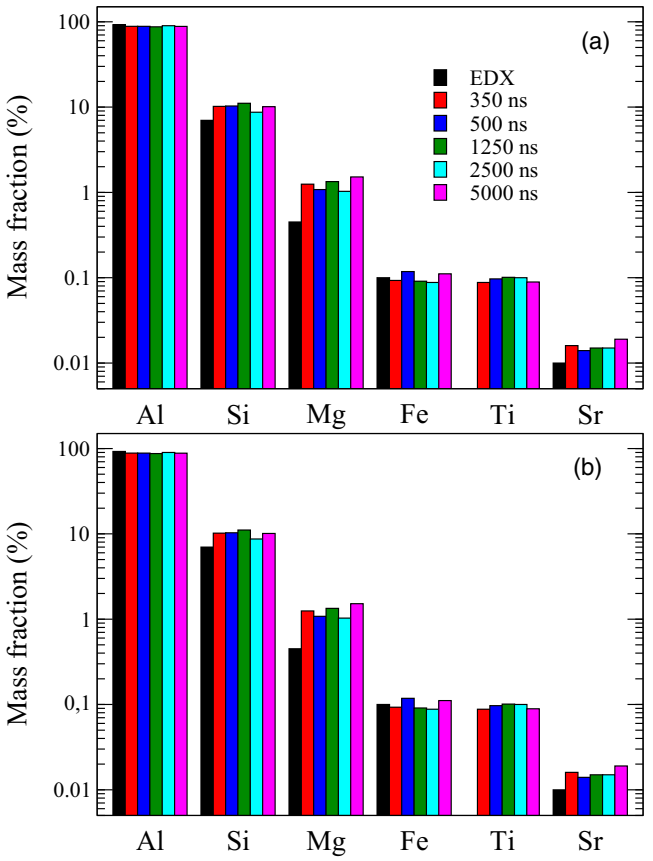

FIG. 13. (Color online) Composition of the aluminum alloy deduced from the analysis of spectra recorded for different gate delays [colored (gray) columns] for laser ablation in argon (a) and air (b). The black columns represent the mass fractions obtained by XRF measurements. Titanium was not detected by XRF.

close to the reference values. For larger delays, the measured fractions deviate from the reference values. The overestimation of the oxygen fraction and thus the underestimation of metal fractions progressively increase with the recording delay. A similar behavior was previously observed in calibration-free

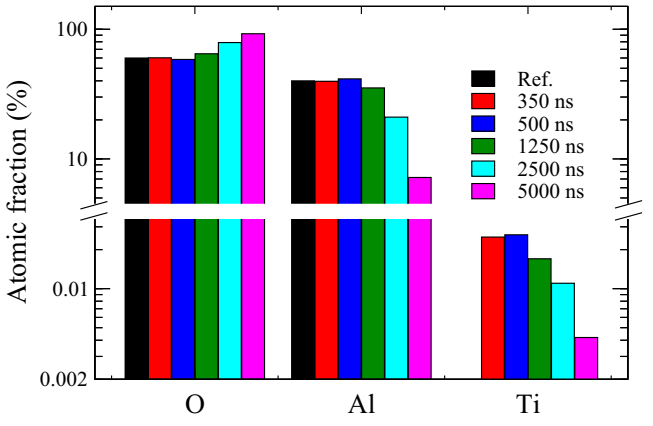

FIG. 14. (Color online) Composition of the Ti-sapphire sample deduced from the analysis of spectra recorded for different gate delays [colored (gray) columns] for laser ablation in argon. The black columns represent the atomic fractions expected for stoichiometric Al_2O_3. The titanium content was unknown.

LIBS analysis of fused silica where accurate measurements were only obtained for spectra recording delays $\leqslant 1$ μs. The overestimation of the oxygen fraction and the increasing mismatch with the recording time were attributed to the failure of local thermodynamic equilibrium. According to the McWhirter criterion, Boltzmann equilibrium distributions of oxygen atoms or ions are only established if $n_e > 10^{17}$ cm^{-3}. For metallic species, much lower n_e values are required to ensure equilibrium distributions [97]. Thus the equilibrium in laser-induced plasmas has a relatively long lifetime for metals, as illustrated by the accuracy of the LIBS analysis for different spectra recording delays (see Fig. 13).

V. CONCLUSION

Using simplified analytical solutions of the radiation transport equation, we demonstrate that emission spectra of plumes produced by ablation of aluminum and Ti-sapphire with UV nanosecond laser pulses are well described by the spectral radiance of a plasma in local thermodynamic equilibrium. The simulations of the emission spectra show that the plasma generated in argon background pressure is almost uniform, whereas temperature and density gradients are observed for ablation in air. Furthermore, the chemical reactions leading to the formation of AlO radicals occur exclusively in the cold plume periphery of the nonuniform plasma in air. For that zone, located between the hot plasma core and the cold background gas, the slight departure from equilibrium is indicated by the small difference between the kinetic temperatures of electrons and heavy particles. Due to the larger electron density, the plasma core is supposed to be in local thermodynamic equilibrium for a duration that depends on the elemental composition. The time-limited validity of LTE is evidenced by the deduction of the elemental composition from the spectra simulation. For aluminum, the composition of the alloy was retrieved from the analysis of spectra recorded in air and argon for delays up to several microseconds. Contrarily, calibration-free analysis of Ti-sapphire was only possible for delays $\leqslant 1$ μs. As the cold plume periphery mostly contributes to the atomic emission spectrum through absorption, it can be ignored in calibration-free LIBS analysis as long as optically thin lines are used and interferences with strongly absorbing atomic lines or molecular bands can be avoided. Finally, we stress that the extrapolation of the here presented scenario to other chemical reactions is possible if the involved molecules have dissociation energies similar to that of AlO. Chemical species of larger dissociation energies such as CO, CN, or NO may have significant number densities in the hot plasma core and calibration-free analysis of organic materials may fail if chemical reactions are ignored.

ACKNOWLEDGMENTS

This research has received funding from LASERLAB-EUROPE (Grant Agreements No. 228334 and No. 284464, Projects CNRS-LP3001733 and CNRS-LP3001877, 7th Framework Programme of European Union) and from the French Environment and Energy Management Agency (ADEME) under Contract No. 0874C0135. This work was also supported by the Istituto Nazionale di Fisica Nucleare (INFN).

[1] L. J. Radziemski and D. A. Cremers, *Laser-Induced Plasmas and Applications* (Marcel Dekker, New York, 1989).
[2] D. H. Gili and A. A. Dougal, Phys. Rev. Lett. **15**, 845 (1965).
[3] R. G. Meyerand and A. F. Haught, Phys. Rev. Lett. **13**, 7 (1964).
[4] R. C. Rosan, M. K. Healy and W. F. McNary Jr., Science **142**, 236 (1963).
[5] A. I. Barchukov, F. V. Bunkin, V. I. Konov, and A. A. Lyubin, Zh. Eksp. Teor. Fiz. **66**, 965 (1974) [Sov. Phys. JETP **39**, 469 (1974)].
[6] M. von Allmen and A. Blatter, *Laser-Beam Interactions with Materials* (Springer, Berlin, 1987).
[7] J. T. Cheung and H. Sankur, Crit. Rev. Solid State Mater. Sci. **15**, 63 (1988).
[8] C. Boulmer-Leborgne, J. Hermann, B. Dubreuil, P. Brault, M. L. DeGiorgi, G. Leggieri, A. Luches, M. Martino, A. Perrone, I. N. Mihailescu, I. Ursu, G. Blondiaux, J. L. Debrun, H. Eestrade, and B. Rousseau, Appl. Surf. Sci. **54**, 349 (1992).
[9] A. C. Tam, W. P. Leung, W. Zapka, and W. Ziemlich, J. Appl. Phys. **71**, 3515 (1992).
[10] D. B. Geohegan, Thin Solid Films **220**, 138 (1992).
[11] R. K. Singh and J. Narayan, Phys. Rev. B **41**, 8843 (1990).
[12] J. C. S. Kools, T. S. Baller, S. T. Dezwart, and J. Dieleman, J. Appl. Phys. **71**, 4547 (1992).
[13] Z. Y. Chen and A. Bogaerts, J. Appl. Phys. **97**, 063305 (2005).
[14] A. V. Bulgakov and N. M. Bulgakova, J. Phys. D: Appl. Phys. **31**, 693 (1998).
[15] I. N. Mihailescu and J. Hermann, in *Laser Processing of Materials*, edited by P. Schaaf (Springer, Berlin, 2010), pp. 49–88.
[16] J. C. S. Kools, J. Appl. Phys. **74**, 6401 (1993).
[17] L. V. Zhigilei, P. B. S. Kodali, and B. J. Garrison, J. Phys. Chem. B **101**, 2028 (1997).
[18] T. E. Itina, J. Hermann, P. Delaporte, and M. Sentis, Phys. Rev. E **66**, 066406 (2002).
[19] L. I. Sedov, *Similarity and Dimensional Methods in Mechanics* (Academic, London, 1959).
[20] D. B. Geohegan and A. A. Puretzky, Appl. Phys. Lett. **67**, 197 (1995).
[21] C. Schäfer, H. M. Urbassek, and L. V. Zhigilei, Phys. Rev. B **66**, 115404 (2002).
[22] W. Sdorra and K. Niemax, Spectrochim. Acta, Part B **45**, 917 (1990).
[23] A. J. Effenberger and J. R. Scott, Sensors **10**, 4907 (2010).
[24] M. A. Gondal and A. A. I. Khalil, Laser Phys. **22**, 1771 (2012).
[25] S. S. Harilal, C. V. Bindhu, V. P. N. Nampoori, and C. P. G. Vallabhan, Appl. Phys. Lett. **72**, 167 (1998).
[26] Z. Wang, T.-B. Yuan, S.-L. Lui, Z.-Y. Hou, X.-W. Li, Z. Li, and W.-D. Ni, Front. Phys. **7**, 708 (2012).
[27] J. A. Merten, E. Ewusi-Annan, B. W. Smith, and N. Omenetto, J. Anal. At. Spectrom. **29**, 571 (2014).
[28] J. Hermann, C. Gerhard, E. Axente, and C. Dutouquet, Spectrochim. Acta, Part B **100**, 189 (2014).
[29] V. Lazic, R. Barbini, F. Colao, R. Fantoni, and A. Palucci, Spectrochim. Acta, Part B **56**, 807 (2001).
[30] M. Cirisan, M. Cvejić, M. R. Gavrilović, S. Jovicević, N. Konjević, and J. Hermann, J. Quant. Spectrosc. Radiat. Transfer **133**, 652 (2014).
[31] J. A. Aguilera, J. Bengoechea, and C. Aragón, Spectrochim. Acta, Part B **59**, 461 (2004).
[32] S.-J. J. Tsai, S.-Y. Chen, Y.-S. Chung, and P.-C. Tseng, Anal. Chem. **78**, 7432 (2006).
[33] V. Motto-Ros, Q. L. Ma, S. G. W. Q. Lei, X. C. Wang, F. Pelascini, F. Surma, V. Detalle, and J. Yu, Spectrochim. Acta, Part B **74-75**, 11 (2012).
[34] X. Bai, Q. Ma, V. Motto-Ros, J. Yu, D. Sabourdy, L. Nguyen, and A. Jalocha, J. Appl. Phys. **113**, 013304 (2013).
[35] E. Tognoni, G. Cristoforetti, S. Legnaioli, and V. Palleschi, Spectrochim. Acta, Part B **65**, 1 (2010).
[36] P. Yaroshchyk, D. Body, R. J. S. Morrison, and B. L. Chadwick, Spectrochim. Acta, Part B **61**, 200 (2006).
[37] S. M. Pershin, F. Colao, and V. Spizzichino, Laser Phys. **16**, 455 (2006).
[38] R. Wester and R. Noll, J. Appl. Phys. **106**, 123302 (2009).
[39] S. Beldjilali, D. Borivent, L. Mercadier, E. Mothe, G. Clair, and J. Hermann, Spectrochim. Acta, Part B **65**, 727 (2010).
[40] I. B. Gornushkin and U. Panne, Spectrochim. Acta, Part B **65**, 345 (2010).
[41] A. D. Giacomo, Spectrochim. Acta, Part B **66**, 661 (2011).
[42] D. W. Hahn and N. Omenetto, Appl. Spectrosc. **66**, 347 (2012).
[43] A. Ciucci, M. Corsi, V. Palleschi, S. Rastelli, A. Salvetti, and E. Tognoni, Appl. Spectrosc. **53**, 960 (1999).
[44] D. Bulajic, M. Corsi, G. Cristoforetti, S. Legnaioli, V. Palleschi, A. Salvetti, and E. Tognoni, Spectrochim. Acta, Part B **57**, 339 (2002).
[45] I. B. Gornushkin, A. Y. Kazakov, N. Omenetto, B. W. Smith, and J. D. Winefordner, Spectrochim. Acta, Part B **60**, 215 (2005).
[46] C. A. D'Angelo, D. M. D. Pace, G. Bertuccelli, and D. Bertuccelli, Spectrochim. Acta, Part B **63**, 367 (2008).
[47] E. Axente, J. Hermann, G. Socol, L. Mercadier, S. A. Beldjilali, M. Cirisan, C. R. Luculescu, C. Ristoscu, I. N. Mihailescu, and V. Craciun, J. Anal. At. Spectrom. **29**, 553 (2014).
[48] S. V. Shabanov and I. B. Gornushkin, Spectrochim. Acta, Part B **100**, 147 (2014).
[49] X. Z. Zhao, L. J. Shen, T. X. Lu, and K. Niemax, Appl. Phys. B **55**, 327 (1992).
[50] Q. Ma, V. Motto-Ros, F. Laye, J. Yu, W. Lei, X. Bai, L. Zheng, and H. Zeng, J. Appl. Phys. **111**, 053301 (2012).
[51] Z.-M. Peng, Y.-J. Ding, X.-D. Zhai, Q.-S. Yang, and Z.-L. Jiang, Chin. Phys. Lett. **28**, 044703 (2011).
[52] W. L. Yip, E. Mothe, S. Beldjilali, and J. Hermann, J. Appl. Phys. **111**, 063108 (2012).
[53] A. De Giacomo, M. Dell'Aglio, O. D. Pascale, R. Gaudiuso, V. Palleschi, C. Parigger, and A. Woods, Spectrochim. Acta, Part B **100**, 180 (2014).
[54] M. Dong, X. Mao, J. J. Gonzalez, J. Lu, and R. E. Russo, Anal. Chem. **85**, 2899 (2013).
[55] J. Lam, D. Amans, F. Chaput, M. Diouf, G. Ledoux, N. Mary, K. Masenelli-Varlot, V. Motto-Ros, and C. Dujardin, Phys. Chem. Chem. Phys. **16**, 963 (2014).
[56] C. G. Parigger and J. O. Hornkohl, Spectrochim. Acta, Part A **81**, 404 (2011).
[57] C. Dutouquet, S. Acquaviva, and J. Hermann, Spectrochim. Acta, Part B **56**, 629 (2001).
[58] R. E. Russo, A. A. Bol'shakov, X. Mao, C. P. McKay, D. L. Perry, and O. Sorkhabi, Spectrochim. Acta, Part B **66**, 99 (2011).
[59] M. Boueri, M. Baudelet, J. Yu, X. Mao, S. S. Mao, and R. Russo, Appl. Surf. Sci. **255**, 9566 (2009).
[60] L. Mercadier, J. Hermann, C. Grisolia, and A. Semerok, J. Anal. At. Spectrom. **28**, 1446 (2013).

[61] J. Hermann, C. Boulmer-Leborgne, and D. Hong, J. Appl. Phys. **83**, 691 (1998).
[62] H. R. Griem, *Plasma Spectroscopy* (Academic, New York, 1964).
[63] M. D. Davidson, H. Volten, and A. Donszelmann, Astronomy & Astrophysics **238**, 452 (1990).
[64] P. Hannaford, Microchem. J. **63**, 43 (1999).
[65] A. Kramida, Y. Ralchenko, and J. Reader, *NIST Atomic Spectra Database (version 5.2)* (National Institute of Standards and Technology, Gaithersburg, MD, 2014).
[66] J. C. Pickering, A. P. Thorne, and R. Perez, Astrophys. J., Suppl. Ser. **132**, 403 (2001).
[67] D. E. Blackwell, A. D. Petford, and M. J. Shallis, Mon. Not. R. Astronom. Soc. **186**, 657 (1979).
[68] K. Butler, C. Mendoza, and C. J. Zeippen, J. Phys. B **26**, 4409 (1993).
[69] T. R. O'Brian and J. E. Lawler, Phys. Rev. A **44**, 7134 (1991).
[70] J. R. Fuhr and W. L. Wiese, in *CRC Handbook of Chemistry and Physics*, 79th ed., edited by D. R. Lide (CRC Press, Boca Raton, FL, 1998), pp. 10–88–10–146.
[71] E. H. Pinnnington, R. W. Berends, and M. Lumsden, J. Phys. B **28**, 2095 (1995).
[72] E. Tognoni, V. Palleschi, M. Corsi, G. Cristoforetti, N. Omenetto, I. Gornushkin, B. W. Smith, and J. D. Winefordner, in *Laser-induced Breakdown Spectroscopy*, edited by A. W. Miziolek, V. Palleschi, and I. Schechter (Cambridge University Press, Berlin, 2006), pp. 122–194.
[73] N. Konjević and J. R. Roberts, J. Phys. Chem. Ref. Data **5**, 209 (1976).
[74] G. Herzberg, *Molecular Spectra and Molecular Structure: Spectra of Diatomic Molecules*, 2nd ed. (Van Nostrand Reinhold, London, 1950), Vol. 1.
[75] A. A. Radzig and B. M. Smirnov, *Reference Data on Atoms, Molecules and Ions* (Springer, Berlin, 1985).
[76] I. Kovács, *Rotational Structure in the Spectra of Diatomic Molecules* (Akadémiai Kiadó, Budapest, 1969).
[77] P. Sriramachandran, B. Viswanathan, and R. Shanmugavel, Sol. Phys. **286**, 315 (2013).
[78] B. Rosen, Phys. Rev. **68**, 124 (1945).
[79] A. Lagerqvist, N. E. L. Nilsson, and R. F. Barrow, Proc. Phys. Soc. London, Sect. A **69**, 356 (1956).
[80] K. P. Huber and G. Herzberg, *Molecular Spectra and Molecular Structure: Constants of Diatomic Molecules* (Van Nostrand Reinhold, New York, 1979), Vol. 4.
[81] M. D. Saksena, M. N. Deo, K. Sunanda, S. H. Behere, and C. T. Londhe, J. Mol. Spectrosc. **247**, 47 (2008).
[82] G. Herzberg, *Molecular Spectra and Molecular Structure: Spectra of Diatomic Molecules*, 2nd ed. (Ref. [74]), p. 222.
[83] C. T. Londhe, K. Sunanda, M. D. Saksena, and S. H. Behere, J. Mol. Spectrosc. **263**, 178 (2010).
[84] S. Eliezer, A. D. Krumbein, and D. Salzmann, J. Phys. D: Appl. Phys. **11**, 1693 (1978).
[85] G. Cristoforetti, S. Legnaioli, V. Palleschi, A. Salvetti, and E. Tognoni, Acta, Part B: Atom. Spectrosc. **59**, 1907 (2004).
[86] Y. B. Zel'dovich and Y. P. Raizer, *Physics of Shock Waves and High Temperature Phenomena* (Academic, New York, 1966).
[87] J. Hermann and C. Dutouquet, J. Appl. Phys. **91**, 10188 (2002).
[88] H. R. Griem, Phys. Rev. **128**, 997 (1962).
[89] M. Burger, M. Skočić, M. Ljubisavljević, Z. Nikolić, and S. Djeniže, Eur. Phys. J. D **68**, 223 (2014).
[90] C. Gerhard, J. Hermann, L. Mercadier, L. Loewenthal, E. Axente, C. R. Luculescu, T. Sarnet, M. Sentis, and W. Viöl, Spectrochim. Acta, Part B **101**, 32 (2014).
[91] R. L. Kurucz and E. Peytremann, SAO Special Report No. 362 (1975).
[92] P. L. Smith, C. Heise, J. R. Esmond, and R. L. Kurucz, Atomic spectral line database built from atomic data files from R. L. Kurucz CD-ROM 23, 2011.
[93] G. Cristoforetti, E. Tognoni, and L. A. Gizzi, Spectrochim. Acta, Part B **90**, 1 (2013).
[94] R. Saad, D. L'Hermite, and B. Bousquet, Spectrochim. Acta, Part B **101**, 330 (2014).
[95] J. Lam, V. Motto-Ros, D. Misiak, C. Dujardin, G. Ledoux, and D. Amans, Spectrochim. Acta, Part B **101**, 86 (2014).
[96] R. McWhirter, in *Plasma Diagnostic Techniques*, edited by R. H. Huddlestone (Academic, New York, 1965), pp. 201–264.
[97] G. Travaillé, O. Peyrusse, B. Bousquet, L. Canioni, K. Michel-Le Pierres, and S. Roy, Spectrochim. Acta, Part B **64**, 931 (2009).